

## CHARACTERISTIC MASS IN GALAXY QUENCHING: ENVIRONMENTAL VERSUS INTERNAL EFFECTS

PENGFEI LI<sup>1,2</sup>, HUIYUAN WANG<sup>1,2</sup>, H.J. MO<sup>3</sup>, ENCI WANG<sup>5</sup>, HUI HONG<sup>1,2</sup>*Draft version December 27, 2021*

## ABSTRACT

A clear transition feature of galaxy quenching is identified in the multi-parameter space of stellar mass ( $M_*$ ), bulge to total mass ratio ( $B/T_m$ ), halo mass ( $M_h$ ) and halo-centric distance ( $r/r_{180}$ ). For given halo mass, the characteristic stellar mass ( $M_{*,ch}$ ) for the transition is about one-fifth of that of the corresponding central galaxy, and almost independent of  $B/T_m$ . Once  $B/T_m$  is fixed, the quenched fraction of galaxies with  $M_* < M_{*,ch}$  increases with  $M_h$ , but decreases with  $M_*$  in the inner part of halos ( $r/r_{180} < 0.5$ ). In the outer part ( $r/r_{180} > 0.5$ ), the trend with  $M_h$  remains but the correlation with  $M_*$  is absent or becomes positive. For galaxies above  $M_{*,ch}$  and with  $B/T_m$  fixed, the quenched fraction increases with  $M_*$ , but depends only weakly on  $M_h$  in both the inner and outer regions. At fixed  $B/T_m$  and  $M_*$ , the quenched fraction increases with decreasing  $r/r_{180}$  for galaxies with  $M_* < M_{*,ch}$ , and depends only weakly on  $r/r_{180}$  for galaxies with  $M_* > M_{*,ch}$ . Our finding provides a physically-motivated way to classify galaxies in halos into two classes based on their quenching properties: an ‘upper class’ with  $M_* > M_{*,ch}$  and a ‘lower class’ with  $M_* < M_{*,ch}$ . Environmental quenching is important for ‘lower class’ galaxies, while internal quenching plays the dominating role for the ‘upper class’.

*Subject headings:* galaxies: halos - galaxies: general – methods: observational - methods: statistical

## 1. INTRODUCTION

In the local Universe, galaxies can be divided into two populations according to their star formation activity or rest-frame color (e.g. [Strateva et al. 2001](#); [Baldry et al. 2004](#); [Brinchmann et al. 2004](#); [Wetzel et al. 2012](#)). One resides in the star forming main sequence, where galaxies in general have blue color and disk-like morphology, and the other is the passive or quenched population, in which galaxies have red color, spheroid-like morphology, and little on-going star formation. The quenched population is observed to be present at redshift as high as  $z = 1$  (e.g. [Bell et al. 2004](#); [Ilbert et al. 2013](#); [Muzzin et al. 2013](#); [Tomczak et al. 2014](#); [Barro et al. 2017](#)) and to grow continuously with time, indicating that quenching drives the evolution of the galaxy population over most of the Hubble time.

Many mechanisms have been proposed for the quenching of galaxies. In broad terms, they can be divided into two categories. The first is internal, such as supernova feedback (e.g. [White & Rees 1978](#); [White & Frenk 1991](#); [Murray et al. 2011](#)) and active galactic nuclei (AGN) feedback (e.g. [Croton et al. 2006](#); [Bower et al. 2006](#); [Best et al. 2007](#); [Fabian 2012](#); [Heckman & Best 2014](#); [He et al. 2019](#)), which may disperse inter-stellar media (ISM) or prevent gas from cooling, so as to reduce the cold gas reservoir for star formation, and morphological quenching (e.g. [Martig et al. 2009](#)), in which cold gas disk is stabilized by a massive bulge. The strengths

of these mechanisms are expected to depend on galaxy stellar mass (or bulge mass) and structural properties, so that the fraction of the quenched galaxies (the quenched fraction) is expected to correlate with the stellar mass, bulge mass, and the bulge to total ratio (hereafter  $B/T$ ) of galaxies. This may be the reason why massive, bulge-dominated early type galaxies are usually observed to have low on-going star formation activities. But the explanation of these correlations is not conclusive ([Lilly & Carollo 2016](#)).

The second category is environmental. The processes in this category include ram pressure stripping (e.g. [Gunn & Gott 1972](#); [Abadi et al. 1999](#); [Wang et al. 2015](#)) and tidal stripping (e.g. [Toomre & Toomre 1972](#); [Read et al. 2006](#)), which remove the ISM from galaxies, and strangulation (e.g. [Larson et al. 1980](#); [Balogh et al. 2000](#); [van den Bosch et al. 2008](#); [Weinmann et al. 2009](#); [Peng et al. 2015](#)), a process that cuts off the replenishment of star forming gas. Interaction and merger of a galaxy with other galaxies, which can consume or disperse cold gas by triggering star formation and/or AGN activity (e.g. [Farouki & Shapiro 1982](#); [Moore et al. 1996](#); [Conselice et al. 2003](#); [Cox et al. 2006](#); [Di Matteo et al. 2005](#)), are two other processes in this category. These environmental processes are expected to produce a quenched fraction that depends on environment, such as the mass of the halo that hosts the galaxy, and the distance of the galaxy from the center of its host halo (halo-centric distance). Moreover, since lower-mass galaxies generally have shallower local gravitational potential wells and are more prone to environmental effects, the trend of quenching with galaxy stellar mass produced by environmental processes is expected to be the opposite to that produced by internal processes.

With the advent of large photometric and spectroscopic surveys of galaxies, the star formation properties of galaxies, and their correlation with both internal

<sup>1</sup> CAS Key Laboratory for Research in Galaxies and Cosmology, Department of Astronomy, University of Science and Technology of China, Hefei, Anhui 230026, China; lpfv@mail.ustc.edu.cn, whywang@ustc.edu.cn

<sup>2</sup> School of Astronomy and Space Science, University of Science and Technology of China, Hefei 230026, China

<sup>3</sup> Department of Astronomy, University of Massachusetts, Amherst MA 01003-9305, USA

<sup>5</sup> Department of Physics, ETH Zurich, Wolfgang-Pauli-Strasse 27, CH-8093 Zurich, Switzerland

properties and environment, have been investigated extensively (e.g. Baldry et al. 2006; Weinmann et al. 2006; van den Bosch et al. 2008; Peng et al. 2010; Wetzel et al. 2012; Fang et al. 2013; Woo et al. 2013; Bluck et al. 2014; Knobel et al. 2015; Woo et al. 2015; Wang et al. 2016; Teimoorinia et al. 2016; Liu et al. 2019; Bluck et al. 2020). It is generally believed that the quenching of central galaxies in halos are dominated by internal processes, while halo-specific environment plays important roles only for satellite galaxies (e.g. van den Bosch et al. 2008). However, both observations and numerical simulations have suggested that satellites may evolve in the same way as centrals for several Gyrs after they merge into their host halos (e.g. Wetzel et al. 2012; Shi et al. 2020), indicating that internal quenching still dominate during this period of time. Indeed, internal processes may play an important role even when environmental process starts to operate (Bahé & McCarthy 2015). On the other hand, central galaxies may also be affected by environmental effects. For example, such effects have been invoked to explain the similarities between the centrals of splashback halos and satellites (Hirschmann et al. 2014). The observed ‘galactic conformity’ within halos (Weinmann et al. 2006) and on larger scales (Kauffmann et al. 2013) also indicates that centrals and satellites are subjected to some common environmental effects. Finally, for massive clusters that contain more than one massive galaxy in the central region, the separation between centrals and satellites is artificial. All these suggest that the simple central-satellite dichotomy may be insufficient to account for quenching in the observed galaxy population, and that the correlation between quenching and galaxy properties is the consequence of both internal and environmental processes. Disentangling these processes is, therefore, essential to understanding galaxy quenching.

Recently, Wang et al. (2018c,b,a, 2020) found that galaxies above and below one-fifth of the central galaxy stellar mass exhibit different dependence of the quenched fraction and galaxy size on the halo-centric distance. Based on the relation between central mass and halo mass relation proposed in Yang et al. (2009), Wang et al. (2020) proposed a characteristic stellar mass,

$$M_{*,\text{ch}} = \frac{M_0}{5} \frac{(M_h/M_1)^{\alpha+\beta}}{(1 + M_h/M_1)^\beta} \quad (1)$$

where  $\log_{10}(M_0/M_\odot h^{-2}) = 10.31$ ,  $\log_{10}(M_1/M_\odot h^{-1}) = 11.04$ ,  $\alpha = 0.31$ , and  $\beta = 4.54$ . If such a characteristic mass is real, it will mean that galaxy quenching is not driven simply by the central-satellite dichotomy, but is determined by the interaction between internal and external processes. In this paper, we perform a detailed analysis about the significance of the characteristic stellar mass in multi-parameter space, aiming at distinguishing different quenching processes.

The paper is organized as follows. Section 2 presents galaxy and group catalogs we use, as well as physical quantities we derive from them. In Section 3, we investigate how the quenched population is correlated with various parameters that quantify internal and external effects, focusing on the presence of characteristic stellar mass scales in the quenching population. Finally, we summarize our results in Section 4.

## 2. OBSERVATIONAL DATA

Our galaxy sample is taken from the New York University Value Added Galaxy Catalog (NYU-VAGC; Blanton et al. 2005), which is based on Sloan Digital Sky Survey (SDSS) DR7 (Abazajian et al. 2009). Following the construction of the group catalog (see below), we select galaxies in the redshift range  $z = 0.01-0.2$ , with spectroscopic completeness ( $C$ ) larger than 0.7 and with the  $r$ -band magnitude limit of 17.72 mag. Stellar masses of individual galaxies,  $M_*$  (in unit of  $h^{-2}M_\odot$ ), are obtained by using the relation between the  $(g-r)$  color and the stellar mass-to-light ratio assuming a Kroupa & Weidner (2003) initial mass function (IMF) (Bell et al. 2003). Star formation rates (SFRs) of galaxies, adopted from the MPA-JHU catalog<sup>5</sup>, are estimated from SDSS spectra using an updated version of the method presented in Brinchmann et al. (2004) and a Kroupa IMF. We separate galaxies into a star-forming population and a quenched population in the SFR- $M_*$  space, as described below.

We use the bulge to total mass ratio ( $B/T_m$ ) of a galaxy as an indicator of its morphological type. Extending the work of Simard et al. (2011), Mendel et al. (2014) obtained the bulge+disk decomposition for SDSS images in the  $u, g, r, i$ , and  $z$  bands. They then estimated the bulge and disk stellar masses by modeling the corresponding broadband spectral energy distribution. We adopt the ratios between the bulge mass and the bulge+disk mass given in Mendel et al. (2014) as the  $B/T_m$  for our sample galaxies. We note that we have made tests using the bulge-to-total light ratio in the  $r$ -band, as given in Simard et al. (2011), instead of  $B/T_m$ , and found no significant changes in our results.

The group catalog used here is constructed by using the halo-based group finder of Yang et al. (2007). The host halo mass ( $M_h$ ) of each group is estimated using a abundance matching method based on the total stellar mass of all member galaxies brighter than  $M_r = -19.5 + 5 \log h$  in the  $r$ -band. Tests using realistic mock catalogs show that the uncertainty in the halo mass estimate is typically 0.2-0.3 dex (Yang et al. 2007; Lim et al. 2017), which is comparable to or smaller than the scales we use to smooth the data. We note that similar smoothing scales are also adopted for stellar masses of galaxies to account for potential uncertainties in  $M_*$ . The most massive galaxy in a group is defined as the central galaxy of the group while all the rest (if any) as satellite galaxies. For each member galaxy in a group, we define a halo-centric distance,  $r/r_{180}$ , where  $r$  is the projected distance between the galaxy and the luminosity-weighted center of the group. The halo virial radius,  $r_{180}$ , is estimated using equation (5) in Yang et al. (2007). Modeling gravitational lensing effects of the groups in Yang et al. (2007), Luo et al. (2018) found that the uncertainties in the group centers are typically within 20% of  $r_{180}$ . We thus choose  $\Delta r/r_{180} = 0.2$  to smooth the data for our analysis.

A total of 23,051 galaxies that do not have estimates of star formation rate or bulge-to-total ratio are discarded from our analysis. Since we want to study the dependence of quenching on halo environment, we only

<sup>5</sup> <http://www.mpa-garching.mpg.de/SDSS/DR7/>

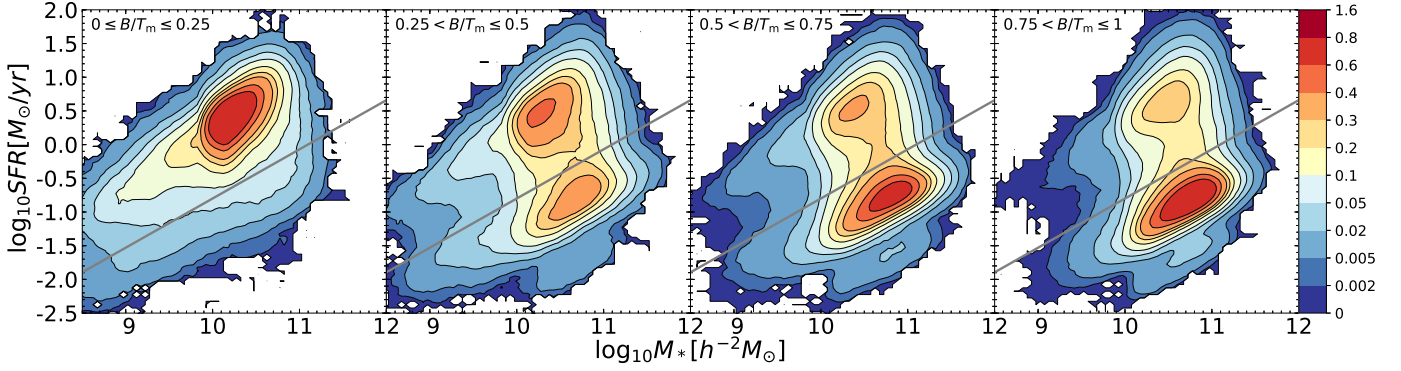


FIG. 1.— The contours show the probability density of galaxies in the  $\log(M_*)$ - $\log(\text{SFR})$  space in four  $B/T_m$  bins as indicated in each panel. The gray line shows the demarcation line proposed by Bluck et al. (2016) to separate star-forming and quenched populations.

use galaxies for which host halo masses are available from Yang et al. (2007). The lowest halo mass is about  $\log(M_h/h^{-1}M_\odot) \sim 11.6$ . We therefore only select galaxies with  $\log(M_h/h^{-1}M_\odot) \geq 11.6$ . This eliminates 94,504 low-mass galaxies, and our final sample contains 426,521 galaxies.

Figure 1 shows the distributions in the SFR- $M_*$  space for our sample galaxies in four  $B/T_m$  bins. The distribution is clearly bimodal for the three high  $B/T$  bins, and the demarcation line proposed by Bluck et al. (2016) can be used to separate the star-forming and quenched populations. This separation is reliable as long as the demarcation line does not cut into one of the modes significantly. For the lowest  $B/T_m$  bin, however, the bimodality is rather weak, and so the definition of a quenched fraction is uncertain (see also Morselli et al. 2017). We use the same demarcation line for the lowest  $B/T_m$  bin, but keep in mind this uncertainty.

### 3. THE CHARACTERISTIC STELLAR MASS

The statistical quantity investigated here is the quenched fraction, defined as the fraction of galaxies that are quenched according to the criterion described above. For a given sub-sample of  $N$  galaxies, the quenched fraction,  $f_Q$ , is calculated as:

$$f_Q = \frac{\sum_{i=1}^N \omega_i q_i}{\sum_{i=1}^N \omega_i}, \quad (2)$$

where  $q_i$  is the quenching property for the  $i$ th galaxy and  $\omega_i$  is a weight assigned to the galaxy. If a galaxy is quenched,  $q_i = 1$ , otherwise  $q_i = 0$ . The weight is defined as  $\omega = 1/(V_{\text{max}}C)$ . Here  $V_{\text{max}}$ , calculated using the  $K$ -correction utilities, v4.2, of Blanton & Roweis (2007), is used to correct for the Malmquist bias, and  $C$  is the redshift incompleteness obtained from the NYU-VAGC.

To start with we first examine how the quenched fraction depends on the two intrinsic properties of galaxies, the stellar mass,  $M_*$  and the bulge-to-total ratio,  $B/T_m$ . Figure 2 shows  $f_Q$  as a function of  $M_*$  for galaxies with different  $B/T_m$  residing in halos with  $\log(M_h/h^{-1}M_\odot) \geq 11.6$ . There is a clear transition in the  $M_*$ -dependence of  $f_Q$ : the quenched fraction first decreases with  $M_*$  at  $\log(M_*/h^{-2}M_\odot) < 10.3$ , and then increases with  $M_*$  at larger masses. This behavior is observed in all  $B/T_m$  bins. Bluck et al. (2014) showed a similar plot in their

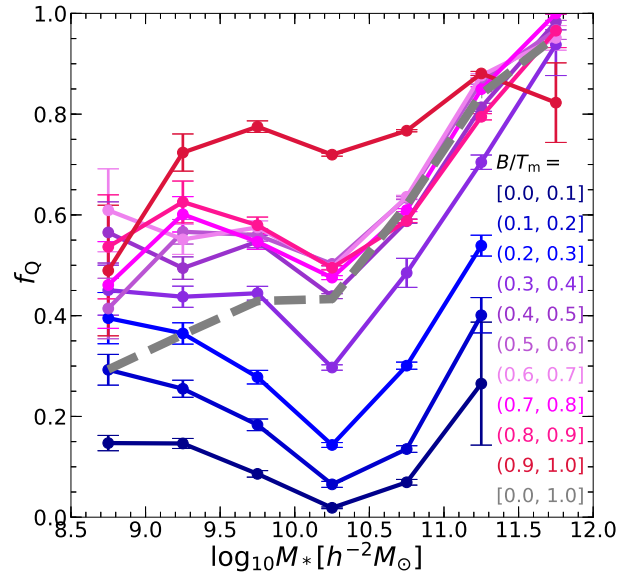


FIG. 2.— Quenched fraction,  $f_Q$ , as a function of  $M_*$  for galaxies of different  $B/T_m$ . Here we only use galaxies residing in halos of  $\log(M_h/h^{-1}M_\odot) \geq 11.6$ , the mass limit of the group sample. Different colors represent different  $B/T_m$ . The grey dashed line shows the result for the whole galaxy sample without separations according to  $B/T_m$ . Bins containing less than 10 galaxies are not used. Error bars are estimated by using 1,000 bootstrap samples.

figure 12, but found no transition in the  $f_Q$ - $M_*$  relation. This is because they included galaxies residing in halos with  $\log(M_h/h^{-1}M_\odot) < 11.6$ . These galaxies are predominantly low-mass, star forming galaxies, and including them decreases  $f_Q$  at the low-mass end. Furthermore, we found that the transition disappears if we lump galaxies with different  $B/T_m$  together, as shown by the grey dashed line in Figure 2 (see also the results in Wang et al. (2018c) and Wang et al. (2018b)). This owes to the fact that galaxies of lower masses have, on average, smaller  $B/T_m$ . Thus, for the whole sample, the results for low-mass and high-mass populations are dominated by galaxies with small and high  $B/T_m$ , respectively. The transitional feature seen for galaxies at fixed  $B/T_m$  is erased by the correlation between  $B/T_m$  and  $M_*$ .

Clearly, using  $M_*$  and  $B/T_m$  alone is not sufficient to understand the origin of the quenched fraction; to achieve this we need to examine how the quenched fraction de-



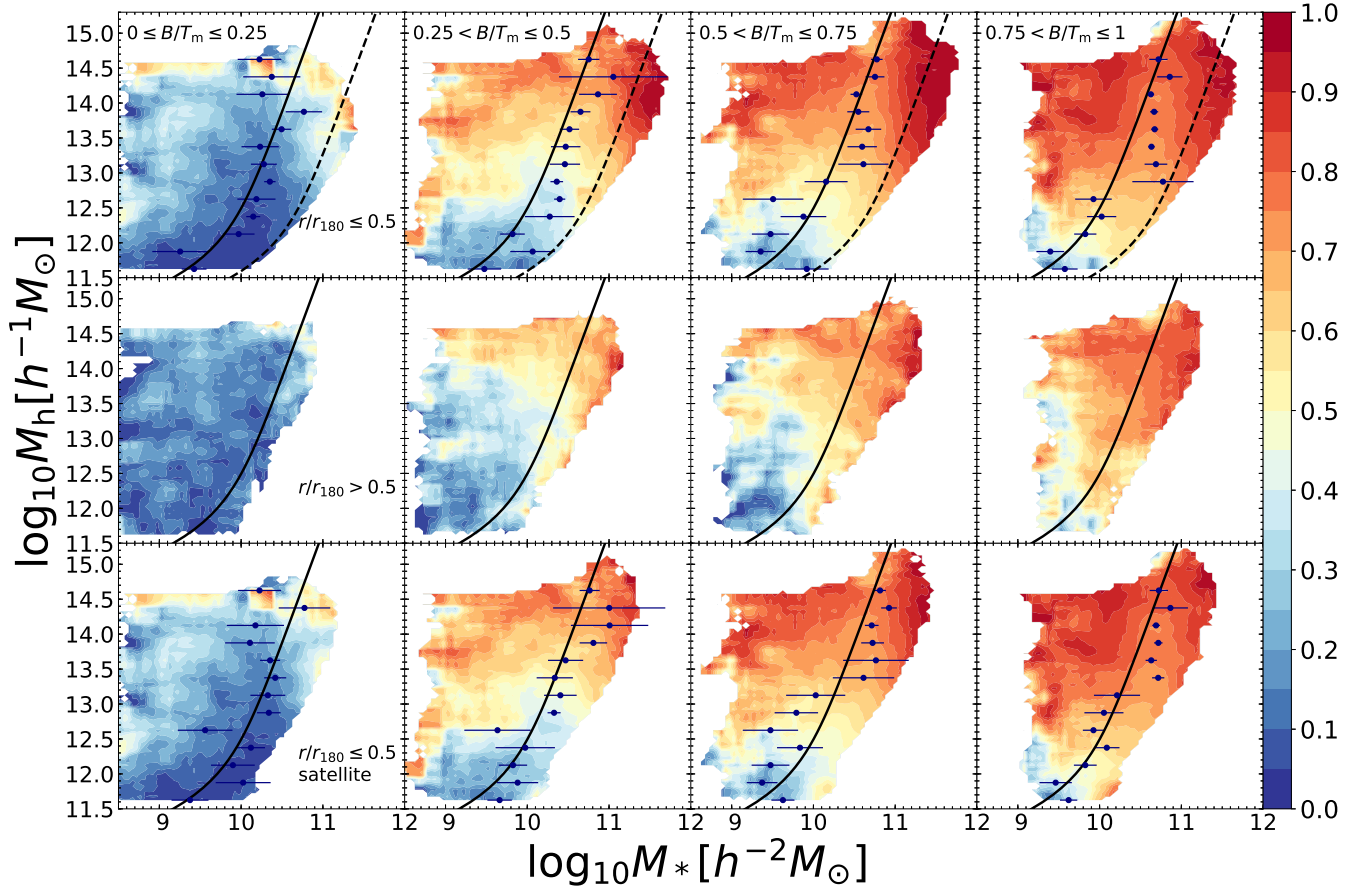


FIG. 3.— Contours show  $f_Q$  as a function of  $M_h$  and  $M_*$ . The top panels are for galaxies with  $r/r_{180} \leq 0.5$ , the middle panels for  $r/r_{180} > 0.5$ , and the bottom panels for satellites with  $r/r_{180} \leq 0.5$ . Different columns show different  $B/T_m$ , as indicated in the top panels. The results shown are smoothed on a grid with cell size given by  $\Delta \log(M_*/h^{-2}M_\odot) = 0.3$  and  $\Delta \log(M_h/h^{-1}M_\odot) = 0.3$ , but our results are insensitive to changes in the smoothing cell size. Cells with less than 10 galaxies are discarded. Solid dots with error bars show the best-fitting  $M_{*,ch}$  and the black solid line shows equation (1). The dashed line in each of the four top panels shows the central mass versus halo mass relation given in Yang et al. (2009).

depends on parameters representing both internal and external processes. Figure 3 shows  $f_Q$  as a function of  $M_h$  and  $M_*$  for galaxies of different  $B/T_m$  located both in the inner ( $r/r_{180} \leq 0.5$ ) and outer ( $r/r_{180} > 0.5$ ) regions of halos. We note that, without separating galaxies according to  $r/r_{180}$ , the results are very similar to those for  $r/r_{180} \leq 0.5$ , and that the choice of  $r/r_{180} = 0.5$  for the separation of inner and outer regions is arbitrary. A valley-like structure in the  $f_Q$  field across the  $M_h$ - $M_*$  plane can clearly be seen for galaxies in the inner region and for almost all samples of  $B/T_m$ . To the left of the valley, the value of  $f_Q$  exhibits a negative correlation with  $M_*$  but a positive correlation with  $M_h$ . To the right of the valley, in contrast,  $f_Q$  shows a strong, positive correlation with  $M_*$  but only weak dependence on  $M_h$ . The transition feature shown in Figure 2 is clearly seen here for halos of different masses. This suggests a systematic change of the importance of environmental versus internal effects as galaxies move across the valley, as we will discuss later.

The stellar mass at the transition depends on  $M_h$ , suggesting the existence of a characteristic stellar mass in

quenching that is related to halo mass. We plot in the upper panels of Figure 3 the demarcation line (equation 1) proposed by Wang et al. (2020) based on the relation of galaxy size with  $r/r_{180}$ . Remarkably, the curve lies close to the bottom of the valley-like structure. To quantify this, we measure  $M_{*,ch}$  as a function of  $M_h$  directly from our data. The results in Figure 2 suggest that  $f_Q$  as a function of  $M_*$  can be approximated by a broken power law. We thus use the following function to model the relation:

$$f_Q = \begin{cases} a \log M_*/M_{*,ch}(M_h) + d, & (M_* < M_{*,ch}) \\ b \log M_*/M_{*,ch}(M_h) + d, & (M_* \geq M_{*,ch}), \end{cases} \quad (3)$$

where  $a$ ,  $b$ ,  $d$  and  $M_{*,ch}$  are free parameters to be determined. The least square method is adopted to perform the fitting and the best-fitting  $M_{*,ch}$  are shown in Figure 3, with error bars estimated using 1000 bootstrap samples.

In general, the best-fitting  $M_{*,ch}$  can characterize the trend of the valley-like structure, suggesting that the measurement is reliable. The measured  $M_{*,ch}$ - $M_h$  relation also matches Equation (1) very well, except in a

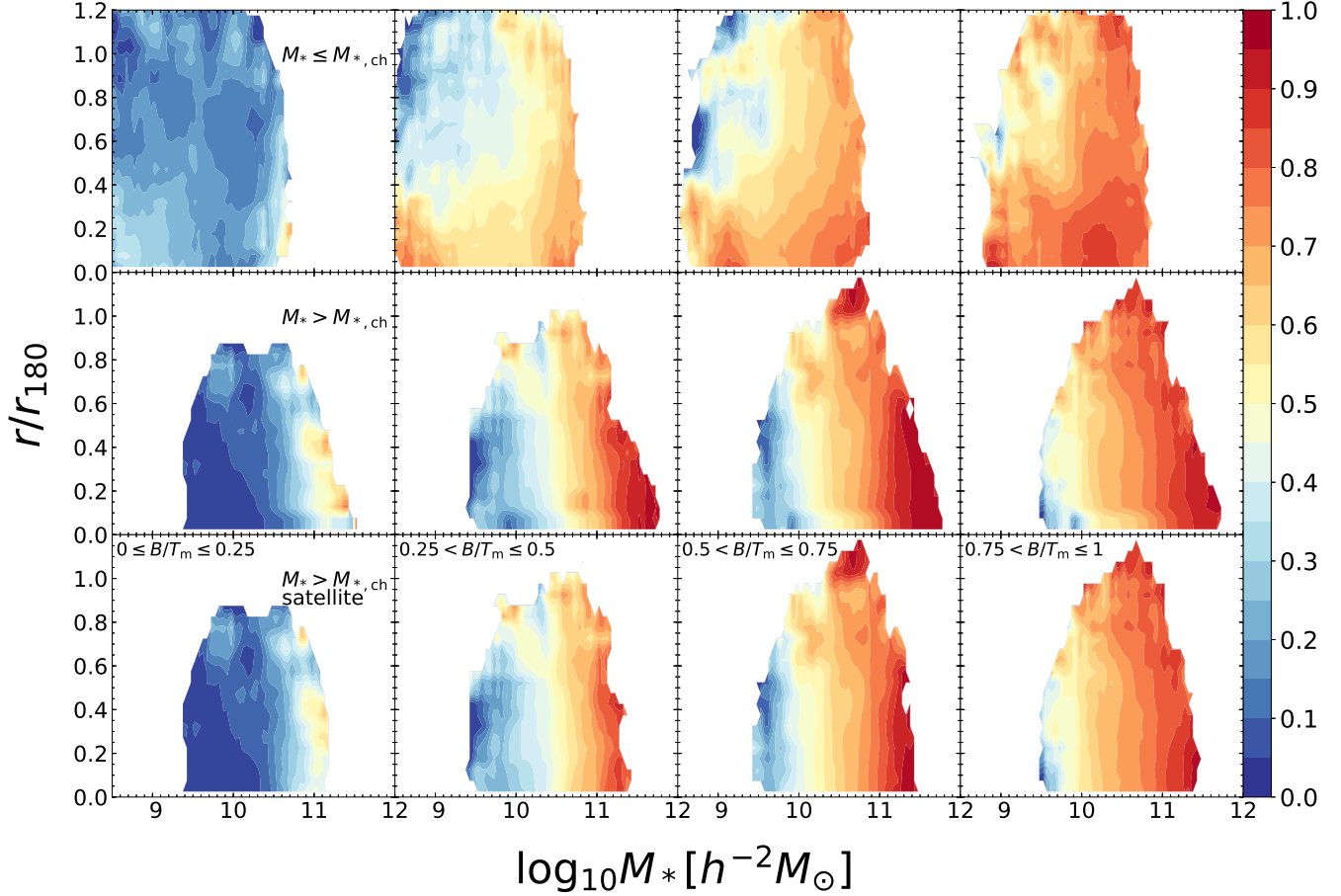


FIG. 4.—  $f_Q$  as a function of  $r/r_{180}$  and  $M_*$ . The top panels show galaxies with  $M_* < M_{*,ch}$ , the middle panels show galaxies with  $M_* > M_{*,ch}$  and the bottom panels show satellites with  $M_* > M_{*,ch}$ . Different columns correspond to different  $B/T_m$ . The grid cell size used in the plot is given by  $\Delta \log(M_*/h^{-2}M_\odot) = 0.3$  and  $\Delta r/r_{180} = 0.2$ ; the results are insensitive to changes in the cell size. Cell containing less than 10 galaxies are discarded.

small number of bins. This indicates that Equation (1) is a good approximation for  $M_{*,ch}(M_h)$ . The fitting results also show that the  $M_{*,ch}-M_h$  relation is similar for different  $B/T_m$ . This is consistent with the results shown in Figure 2, where the values of  $M_{*,ch}$  averaged over different  $M_h$  are all close to  $10^{10.3} h^{-2} M_\odot$  for different  $B/T_m$ . However, it is also clear that  $M_{*,ch}$  increases with  $M_h$ . For Milky-Way size halos,  $M_{*,ch} \sim 10^{9.7} h^{-2} M_\odot$ , while for rich clusters,  $M_{*,ch} \sim 10^{10.7} h^{-2} M_\odot$ .

We also show Equation (1) in the mid-row panels of Figure 3. Although a valley-like structure is not obvious here, galaxies to the left and right of the curve do exhibit different behavior. For example, to the left of the curve, the correlation with  $M_*$  is weak at small  $B/T_m$  and positive at large  $B/T_m$ . To the right of the curve, on the other hand,  $f_Q$  increases with  $M_*$  much more rapidly. More importantly, the  $M_h$  dependence is strong on the left side of the curve, but is weak or absent on the right.

One possible origin of the transition is the central-satellite dichotomy. If centrals behave very differently from satellites, a transition feature might be produced. We therefore show the central mass - halo mass relation obtained by (Yang et al. 2009) as the dashed lines in the upper-row panels to indicate where central galaxies are

likely to be located in the  $M_*-M_h$  space. Since the stellar mass - halo mass relation for centrals is quite tight and quite far away from  $M_{*,ch}-M_h$  relation, one expects that the transition feature is dominated by satellite galaxies. To demonstrate this directly, the bottom row of Figure 3 shows the contour plots of the quenched fraction of satellites galaxies, together with the best-fitting  $M_{*,ch}$ . The transition feature is also clearly seen for satellites in all the  $B/T_m$  bins, and the best-fitting  $M_{*,ch}$  matches Equation (1). This indicates that the characteristic mass we obtain is not produced by the central-satellite dichotomy.

Given the difference in behavior for galaxies below and above  $M_{*,ch}$ , it is interesting to investigate whether or not the two populations have different dependence on  $r/r_{180}$ . For NFW halos (Navarro et al. 1997),  $r/r_{180}$  is an approximate measure of the local mass density, independent of halo mass, and so can be used as an indicator of local environment within individual halos. Figure 4 shows  $f_Q$  as a function of  $r/r_{180}$  and  $M_*$  for galaxies of different  $B/T_m$ . For galaxies with  $M_* \geq M_{*,ch}$ ,  $f_Q$  decreases with increasing  $r/r_{180}$ , indicating that such galaxies tend to be more quenched in the inner region. In contrast, the  $r/r_{180}$  dependence is almost absent for  $M_* < M_{*,ch}$ . The results remain basically the same after

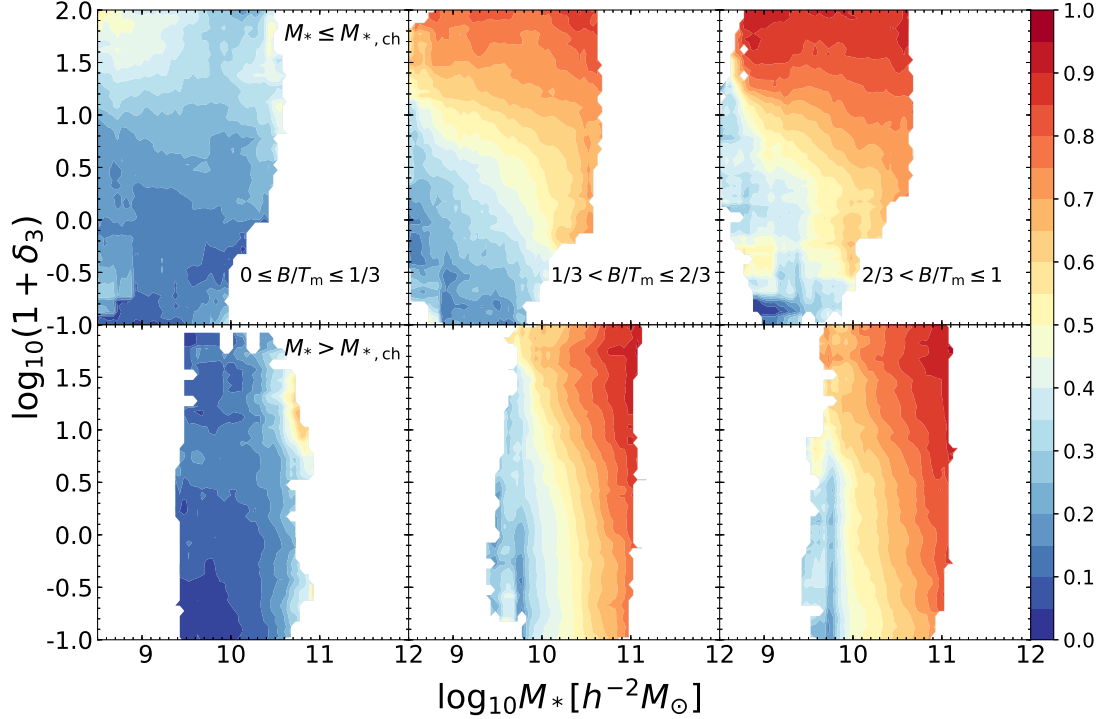


FIG. 5.— Contours show  $f_Q$  as a function of  $\log(1 + \delta_3)$  and  $M_*$ . Upper panels show results for galaxies in the upper class, i.e. with  $M_* \leq M_{*,\text{ch}}$ , while lower panels show results for  $M_* > M_{*,\text{ch}}$ . Different columns correspond to different  $B/T_m$ . Results are shown for galaxies with  $0.01 < z < 0.05$ . The grid cell size used in the plot is given by  $\Delta \log(M_*/h^{-2}M_\odot) = 0.6$  and  $\Delta \log(1 + \delta_3) = 0.6$ ; the results are insensitive to changes in the cell size. Cells containing less than 10 galaxies are discarded.

central galaxies are eliminated, as shown in the bottom row of Figure 4.

Note that we do not distinguish halos of different masses in the results shown Figure 4. One might think that the results shown above are caused by the dependence on halo mass. However, as shown in Yang et al. (2005), the distribution of satellite galaxies traces the dark matter profile in a similar way in groups of different masses. In fact, Wang et al. (2018c) and Wang et al. (2018b) found that, for galaxies of given stellar mass, the quenched fraction is independent of  $r/r_{180}$  for  $M_* > M_{*,\text{ch}}$  and decreases with  $r/r_{180}$  for  $M_* < M_{*,\text{ch}}$ , and that this is true even when the host halo mass is controlled. Our test using galaxies within several halo mass bins, as shown in Figure 7 in the Appendix, confirms that the  $r/r_{180}$  dependence is not produced by the dependence on halo mass. Thus, the dependence on  $r/r_{180}$  provide independent evidence that the characteristic mass,  $M_{*,\text{ch}}$ , defines a boundary where environmental effects start to play an important role in galaxy quenching.

A kink-like structure in the contours of  $f_Q$  is noticeable at the high stellar mass edge for galaxies in upper panels of Figure 3 and at  $r/r_{180} \sim 0$  in the middle panels of Figure 4. Their high stellar mass for their halo mass and their small halo-centric distance suggest that these galaxies are dominated by centrals. Indeed, the structure disappears if centrals are eliminated. Unfortunately, it is unclear if this is a real feature, or a false signal produced by the halo mass assignment technique based on the total stellar mass that is dominated by the most massive galaxies for some groups.

As an independent check of our results on the difference between the upper and lower classes, we use the commonly-adopted nearest neighbour galaxy density (e.g. Baldry et al. 2006; Muldrew et al. 2012) to represent the local environment. To obtain a reliable galaxy density measurement, here we only focus on the low redshift galaxy sample, with  $0.01 \leq z \leq 0.05$ . We have checked our results using  $0.01 \leq z \leq 0.1$  and reached similar conclusions. For each galaxy (target) in the sample, we calculate the local density as  $\Sigma_3 = 3/\pi d_3^2$ , where  $d_3$  is the projected distance of the target to its third nearest neighbour that belongs to a volume-limited sample and has velocity difference less than 1000 km/s with the target. We define a normalized density as  $1 + \delta_3 = \Sigma_3/\bar{\Sigma}_3$ , where  $\bar{\Sigma}_3$  is the median density of all targets in the sample. Figure 5 shows the quenched fraction as a function of  $M_*$  and  $1 + \delta_3$ . As one can see, galaxies below  $M_{*,\text{ch}}$  show strong dependence on  $1 + \delta_3$ , while above  $M_{*,\text{ch}}$  the dependence is much weaker. This is consistent with the results based on  $r/r_{180}$  and  $M_h$ . There is weak but significant dependence of  $f_Q$  on  $\delta_3$  for the upper class galaxies, which is in qualitative agreement with the weak, positive correlation between  $f_Q$  and  $M_h$  seen in Fig. 3.

We conclude this section with some discussion about the uncertainties that may affect our results. As shown in Figure 1, galaxies in the lowest  $B/T_m$  bin lack a clear bimodal distribution in the SFR- $M_*$  space. This makes the separation between the star-forming and quenched populations uncertain. However, as shown above, the transition feature is found for all the  $B/T_m$  bins and the characteristic mass is almost independent of  $B/T_m$ .

This suggests that the use of the same demarcation line for low- $B/T_m$  galaxies is reasonable and that the transition feature seen for galaxies of different  $B/T_m$  may have a similar origin. There are also potential uncertainties introduced by effects like fiber aperture, sample completeness and bulge+disk decomposition, which are expected to be redshift dependent. As a test, we have made the same analysis but using galaxies in smaller redshift ranges,  $0.01 \leq z \leq 0.05$  and  $0.01 \leq z \leq 0.1$ , and the results are presented in the Appendix (see Fig. 6). The transition feature is clearly seen in these results, albeit noisier than that for the whole sample because of the smaller sample size. This demonstrates that the characteristic mass we find is not a result of these uncertainties.

#### 4. SUMMARY AND DISCUSSION

In this paper, we have investigated how galaxy quenching in star formation depends on internal properties of galaxies, represented by their stellar mass and  $B/T_m$ , and on environment, represented by the mass of their host halos and their distances to the halo centers. Our main results can be summarized as follows.

- For a given  $B/T_m$  and a given host halo mass, there is a characteristic stellar mass,  $M_{*,\text{ch}}$ , where  $f_Q$  is the lowest. The characteristic mass is about one-fifth of that of the central galaxy of the halo, almost independent of  $B/T_m$ . The presence of the characteristic mass is more prominent in the inner region of halos.
- Galaxies with masses below and above  $M_{*,\text{ch}}$  have different quenching properties. At  $M_* < M_{*,\text{ch}}$ ,  $f_Q$  for galaxies of a given  $B/T_m$  decreases with  $M_*$  and  $r/r_{180}$  but increases with  $M_h$ . At  $M_* \geq M_{*,\text{ch}}$ , however,  $f_Q$  increases with  $M_*$  but depends only weakly on  $M_h$  and  $r/r_{180}$ . The trend with  $M_h$  is similar in both the inner and outer regions, but the decrease of  $f_Q$  with  $M_*$  at  $M_* < M_{*,\text{ch}}$  is absent in the outer region. Similar conclusions are reached using  $\delta_3$  to represent the environmental density.
- The characteristic stellar mass is independent of the central-satellite dichotomy.

Observationally, the most massive/luminous galaxy in a galaxy groups/clusters is usually classified as the central, while the rest as satellites. As mentioned in the introduction, such classification may not be able to truly reflect the physical processes operating on them. This definition is also different from that in theoretical models and simulations, where a central galaxy usually refers to the one located near the center of the host halo or the bottom of the gravitational potential well. Given that galaxies below and above  $M_{*,\text{ch}}$  have systematically different quenching properties, our finding provides an physically-motivated dichotomy for galaxies in halos, an ‘upper class’ with  $M_* > M_{*,\text{ch}}$  and a ‘lower class’ with  $M_* < M_{*,\text{ch}}$ .

‘Lower class’ galaxies exhibit strong dependence of  $f_Q$  on both  $M_h$  and  $r/r_{180}$  even with both  $M_*$  and  $B/T_m$  controlled (Figs. 3 and 4). This clearly indicates that quenching of these galaxies is strongly affected by environment. Theoretically, many environmental processes, such as ram pressure and tidal stripping, predict a higher

efficiency for galaxies of lower mass, because of their shallower gravitational potential wells. The decrease of  $f_Q$  with  $M_*$  at the low-mass end thus provides a strong evidence for such environmental quenching. The interpretation is not unique though, as the final environmental effect depends not only on the strength of quenching mechanisms, but also on how long these mechanisms operate. For example, Shi et al. (2020) found that satellites accreted earlier by their host halos are more frequently quenched. Thus, if the accretion time for a satellite depends on  $M_h$ ,  $M_*$  and  $r/r_{180}$ , the observed correlations can also be produced even if the strengths of the quenching mechanisms are independent of the three parameters. More investigations are needed to disentangle the dependencies on accretion time and quenching strength.

One interesting property of the ‘lower class’ is that the dependence of  $f_Q$  on  $M_h$  and  $r/r_{180}$  is much stronger for higher  $B/T_m$  galaxies (Figs. 3 and 4). This indicates that environmental processes are more effective in quenching galaxies of higher  $B/T_m$ . One possibility is that the ISM in higher  $B/T_m$  galaxies is more fluffy and easier to strip, as shown in hydrodynamic simulations (Bahé & McCarthy 2015). Another possibility is that galaxies with higher  $B/T_m$  are accreted into their hosts earlier, so that the impact by environment is larger. Indeed, galaxies formed earlier are more compact (Mo et al. 1999; van der Wel et al. 2014) and more likely to become galaxies with higher  $B/T_m$  at  $z = 0$ . In both possibilities, environmental effects may affect the star formation of a galaxy without changing its structure. Thus, unless  $B/T_m$  is created with strong dependence on  $M_h$  and  $r/r_{180}$ , the weak dependence of galaxy morphology on  $M_h$  and  $r/r_{180}$  (Liu et al. 2019) suggests that galaxy morphology may indeed have formed without strong dependence on environment. Our results strongly suggest that galaxy morphology, as represented by  $B/T_m$ , is an important factor in affecting the efficiency of both internal and environmental quenching processes.

For galaxies in the ‘upper class’,  $f_Q$  depends only weakly on  $M_h$ ,  $r/r_{180}$  and  $\delta_3$ , indicating that their quenching is dominated by internal processes. The strong increase of  $f_Q$  with both  $M_*$  and  $B/T_m$  (Figs. 2 and 3) at the massive end provides support to such interpretation, and suggests that the existence of a significant bulge is essential for galaxy quenching (e.g. Bluck et al. 2014). A number of quenching mechanisms linked to galaxy bulge have been proposed. The morphological quenching, proposed in Martig et al. (2009), is expected to predict strong dependence of  $f_Q$  on  $B/T_m$ . However, it is unclear if the model can predict the strong  $M_*$ -dependence at fixed  $B/T_m$ . Various types of AGN feedback models assume that the quenching of massive galaxies is produced by the energy generated by super-massive black holes whose mass is strongly correlated with the velocity dispersion/stellar mass of the bulge (Kormendy & Ho 2013). These models, therefore, predict a strong positive correlation between  $f_Q$  and the bulge mass, as seen in our results. However, there are still uncertainties regarding the strength and mode of AGN feedback, and competing models have been proposed (see e.g. Heckman & Best 2014). Furthermore, star formation associated with the formation of the bulge may also suppress subsequent gas accretion and star formation in the disk (e.g. Mo & Mao 2004). Finally, satellite galaxies in the



‘upper class’ are also subjected to environmental effects. However, because of their large stellar mass, these galaxies may be able to maintain their gas reservoir before merging with the central galaxies, so that environmental effects play only a minor role in quenching their star formation.

The characteristic mass scale is thus a result of the competition between internal and environmental processes. In a halo of a given mass, both processes are expected to have comparable impacts on quenching for galaxies around the characteristic mass. Understanding the origin of the simple relation between  $M_{*,\text{ch}}$  and  $M_h$  obtained here is, therefore, crucial for understanding the nature of both environmental and internal quenching mechanisms.

### ACKNOWLEDGMENTS

We thank the referee for useful comments that significantly improve the paper. This work is supported by the National Key R&D Program of China (grant

No. 2018YFA0404503), the National Natural Science Foundation of China (NSFC, Nos. 11733004, 11421303, 11890693, and 11522324), the National Basic Research Program of China (973 Program)(2015CB857002), and the Fundamental Research Funds for the Central Universities. P.F.L. is supported by the Fund for Fostering Talents in Basic Science of the National Natural Science Foundation of China NO.J1310021. EW is supported by the Swiss National Science Foundation. The work is also supported by the Supercomputer Center of University of Science and Technology of China. This research utilized: NumPy (van der Walt et al. 2011), a fundamental package for scientific computing with Python; SciPy (Jones et al. 2001–), a Python based ecosystem of open software for mathematics, science and engineering; Matplotlib (Hunter 2007), a comprehensive library for creating static, animated and interactive visualizations in Python; Astropy (Price-Whelan et al. 2018), a community python library for astronomy.

### REFERENCES

- Abadi, M. G., Moore, B., & Bower, R. G. 1999, *MNRAS*, 308, 947  
 Abazajian, K. N., Adelman-McCarthy, J. K., Agüeros, M. A., et al. 2009, *ApJS*, 182, 543  
 Bahé, Y. M., & McCarthy, I. G. 2015, *MNRAS*, 447, 969  
 Baldry, I. K., Balogh, M. L., Bower, R. G., et al. 2006, *MNRAS*, 373, 469  
 Baldry, I. K., Glazebrook, K., Brinkmann, J., et al. 2004, *ApJ*, 600, 681  
 Balogh, M. L., Navarro, J. F., & Morris, S. L. 2000, *ApJ*, 540, 113  
 Barro, G., Faber, S. M., Koo, D. C., et al. 2017, *ApJ*, 840, 47  
 Bell, E. F., McIntosh, D. H., Katz, N., & Weinberg, M. D. 2003, *ApJS*, 149, 289  
 Bell, E. F., Wolf, C., Meisenheimer, K., et al. 2004, *ApJ*, 608, 752  
 Best, P. N., von der Linden, A., Kauffmann, G., Heckman, T. M., & Kaiser, C. R. 2007, *MNRAS*, 379, 894  
 Blanton, M. R., & Roweis, S. 2007, *AJ*, 133, 734  
 Blanton, M. R., Schlegel, D. J., Strauss, M. A., et al. 2005, *AJ*, 129, 2562  
 Bluck, A. F. L., Maiolino, R., Sánchez, S. F., et al. 2020, *MNRAS*, 492, 96  
 Bluck, A. F. L., Mendel, J. T., Ellison, S. L., et al. 2014, *MNRAS*, 441, 599  
 —. 2016, *MNRAS*, 462, 2559  
 Bower, R. G., Benson, A. J., Malbon, R., et al. 2006, *MNRAS*, 370, 645  
 Brinchmann, J., Charlot, S., White, S. D. M., et al. 2004, *MNRAS*, 351, 1151  
 Conselice, C. J., Chapman, S. C., & Windhorst, R. A. 2003, *ApJ*, 596, L5  
 Cox, T. J., Jonsson, P., Primack, J. R., & Somerville, R. S. 2006, *MNRAS*, 373, 1013  
 Croton, D. J., Springel, V., White, S. D. M., et al. 2006, *MNRAS*, 365, 11  
 Di Matteo, T., Springel, V., & Hernquist, L. 2005, *Nature*, 433, 604  
 Fabian, A. C. 2012, *ARA&A*, 50, 455  
 Fang, J. J., Faber, S. M., Koo, D. C., & Dekel, A. 2013, *ApJ*, 776, 63  
 Farouki, R. T., & Shapiro, S. L. 1982, *ApJ*, 259, 103  
 Gunn, J. E., & Gott, III, J. R. 1972, *ApJ*, 176, 1  
 He, Z., Wang, T., Liu, G., et al. 2019, *Nature Astronomy*, 3, 265  
 Heckman, T. M., & Best, P. N. 2014, *ARA&A*, 52, 589  
 Hirschmann, M., De Lucia, G., Wilman, D., et al. 2014, *MNRAS*, 444, 2938  
 Hunter, J. D. 2007, *Computing in Science & Engineering*, 9, 90  
 Ilbert, O., McCracken, H. J., Le Fèvre, O., et al. 2013, *A&A*, 556, A55  
 Jones, E., Oliphant, T., Peterson, P., et al. 2001–, *SciPy: Open source scientific tools for Python*  
 Kauffmann, G., Li, C., Zhang, W., & Weinmann, S. 2013, *MNRAS*, 430, 1447  
 Knobel, C., Lilly, S. J., Woo, J., & Kovač, K. 2015, *ApJ*, 800, 24  
 Kormendy, J., & Ho, L. C. 2013, *ARA&A*, 51, 511  
 Kroupa, P., & Weidner, C. 2003, *ApJ*, 598, 1076  
 Larson, R. B., Tinsley, B. M., & Caldwell, C. N. 1980, *ApJ*, 237, 692  
 Lilly, S. J., & Carollo, C. M. 2016, *ApJ*, 833, 1  
 Lim, S. H., Mo, H. J., Lu, Y., Wang, H., & Yang, X. 2017, *MNRAS*, 470, 2982  
 Liu, C., Hao, L., Wang, H., & Yang, X. 2019, *ApJ*, 878, 69  
 Luo, W., Yang, X., Lu, T., et al. 2018, *ApJ*, 862, 4  
 Martig, M., Bournaud, F., Teyssier, R., & Dekel, A. 2009, *ApJ*, 707, 250  
 Mendel, J. T., Simard, L., Palmer, M., Ellison, S. L., & Patton, D. R. 2014, *ApJS*, 210, 3  
 Mo, H. J., & Mao, S. 2004, *MNRAS*, 353, 829  
 Mo, H. J., Mao, S., & White, S. D. M. 1999, *MNRAS*, 304, 175  
 Moore, B., Katz, N., Lake, G., Dressler, A., & Oemler, A. 1996, *Nature*, 379, 613  
 Morselli, L., Popesso, P., Erfanianfar, G., & Concas, A. 2017, *A&A*, 597, A97  
 Muldrew, S. I., Croton, D. J., Skibba, R. A., et al. 2012, *MNRAS*, 419, 2670  
 Murray, N., Ménard, B., & Thompson, T. A. 2011, *ApJ*, 735, 66  
 Muzzini, A., Marchesini, D., Stefanon, M., et al. 2013, *ApJ*, 777, 18  
 Navarro, J. F., Frenk, C. S., & White, S. D. M. 1997, *ApJ*, 490, 493  
 Peng, Y., Maiolino, R., & Cochrane, R. 2015, *Nature*, 521, 192  
 Peng, Y.-j., Lilly, S. J., Kovač, K., et al. 2010, *ApJ*, 721, 193  
 Price-Whelan, A. M., Sipőcz, B. M., Günther, H. M., et al. 2018, *AJ*, 156, 123  
 Read, J. I., Wilkinson, M. I., Evans, N. W., Gilmore, G., & Kleyana, J. T. 2006, *MNRAS*, 366, 429  
 Shi, J., Wang, H., Mo, H., et al. 2020, *ApJ*, 893, 139  
 Simard, L., Mendel, J. T., Patton, D. R., Ellison, S. L., & McConnell, A. W. 2011, *ApJS*, 196, 11  
 Strateva, I., Ivezić, Ž., Knapp, G. R., et al. 2001, *AJ*, 122, 1861  
 Teimoorinia, H., Bluck, A. F. L., & Ellison, S. L. 2016, *MNRAS*, 457, 2086  
 Tomczak, A. R., Quadri, R. F., Tran, K.-V. H., et al. 2014, *ApJ*, 783, 85  
 Toomre, A., & Toomre, J. 1972, *ApJ*, 178, 623  
 van den Bosch, F. C., Aquino, D., Yang, X., et al. 2008, *MNRAS*, 387, 79  
 van der Walt, S., Colbert, S. C., & Varoquaux, G. 2011, *Computing in Science Engineering*, 13, 22  
 van der Wel, A., Franx, M., van Dokkum, P. G., et al. 2014, *ApJ*, 788, 28  
 Wang, E., Wang, H., Mo, H., et al. 2018a, *ApJ*, 864, 51  
 Wang, E., Wang, H., Mo, H., van den Bosch, F. C., & Yang, X. 2020, *ApJ*, 889, 37  
 Wang, E., Wang, J., Kauffmann, G., Józsa, G. I. G., & Li, C. 2015, *MNRAS*, 449, 2010  
 Wang, E., Wang, H., Mo, H., et al. 2018b, *ApJ*, 860, 102  
 Wang, H., Mo, H. J., Yang, X., & van den Bosch, F. C. 2012, *MNRAS*, 420, 1809  
 Wang, H., Mo, H. J., Yang, X., et al. 2016, *ApJ*, 831, 164  
 Wang, H., Mo, H. J., Chen, S., et al. 2018c, *ApJ*, 852, 31  
 Weinmann, S. M., Kauffmann, G., van den Bosch, F. C., et al. 2009, *MNRAS*, 394, 1213



Weinmann, S. M., van den Bosch, F. C., Yang, X., & Mo, H. J. 2006, MNRAS, 366, 2  
Wetzel, A. R., Tinker, J. L., & Conroy, C. 2012, MNRAS, 424, 232  
White, S. D. M., & Frenk, C. S. 1991, ApJ, 379, 52  
White, S. D. M., & Rees, M. J. 1978, MNRAS, 183, 341  
Woo, J., Dekel, A., Faber, S. M., & Koo, D. C. 2015, MNRAS, 448, 237

Woo, J., Dekel, A., Faber, S. M., et al. 2013, MNRAS, 428, 3306  
Yang, X., Mo, H. J., & van den Bosch, F. C. 2009, ApJ, 695, 900  
Yang, X., Mo, H. J., van den Bosch, F. C., et al. 2007, ApJ, 671, 153  
—. 2005, MNRAS, 362, 711

## APPENDIX

Sample completeness, fiber aperture and the uncertainties in bulge+disk decomposition may generate uncertainties in the physical quantities used in our analysis. These effects are usually redshift-dependent. For example, fiber aperture effect is expected to be more significant at lower  $z$  while bulge+disk decomposition and group/galaxy samples may be more uncertain at higher  $z$ . In addition, galaxy groups with  $\log(M_h/h^{-1}M_\odot) = 11.6$  are only complete at  $z < 0.10$ , although more massive groups are complete to higher  $z$  (Yang et al. 2009; Wang et al. 2012). To examine the impact of such effects, we have made tests using galaxies in two narrower redshift ranges,  $0.01 < z \leq 0.05$  and  $0.01 < z \leq 0.1$ . Since the sample size is reduced by using galaxies in a narrower redshift range and since we are considering the quenched fraction in a multi-dimensional space, we have to use larger  $B/T_m$  bins and larger smoothing length to suppress noise. The results are shown in Figure 6. For comparison, the results for the whole sample (i.e.  $0.01 < z < 0.2$ ) analyzed in the same way are shown in the bottom panels. As one can see, the transition feature is clearly seen in all the three  $B/T_m$  bins for the low- $z$  samples. More importantly, the behavior of the transition in the  $(M_*, M_h)$  space is very similar to that for the whole sample. The transition feature for the lowest redshift sample appears to be slightly weaker than that for the other two samples. There are two reasons for this. Firstly, as mentioned above, since the size of this sample is much smaller, the statistic is noisier, particularly for galaxies and groups of high masses whose number densities are low. Indeed, the contours at the upper-right corner are now missing exactly because of the lack of galaxies in this region. Secondly, fiber aperture effect may affect the measurements of star formation rates, although corrections were made for aperture bias in the original data (Brinchmann et al. 2004). The aperture effect is expected to be severer at lower redshift, because of the larger angular sizes of galaxies. We also checked the quenched fraction as a function of  $(r/r_{180}, M_*)$  using the two lower- $z$  samples, and found that all of our conclusions remain unchanged. These test results demonstrate that the transition feature and the characteristic mass are not generated by these effects.

The results shown in Figure 4 do not distinguish halos of different mass. To examine whether or not the dependence on  $r/r_{180}$  shown there is caused by the dependence on halo mass, we show in Figure 7 the quenched fraction as a function of  $r/r_{180}$  and  $M_*$  in three  $M_h$  bins. We use only three  $B/T_m$  bins in order to reduce statistical uncertainties. The vertical band in each panel indicates the range of  $M_{*,\text{ch}}$  covered by the corresponding halo mass bin. As one can see, even within a given halo mass bin, galaxies below and above  $M_{*,\text{ch}}$  have different dependence on  $r/r_{180}$ . The dependence is strong at  $M_* < M_{*,\text{ch}}$ , but rather weak at  $M_* > M_{*,\text{ch}}$ , indicating that the  $r/r_{180}$ -dependence within each class shown in Figure 4 is not caused by the dependence on halo mass.

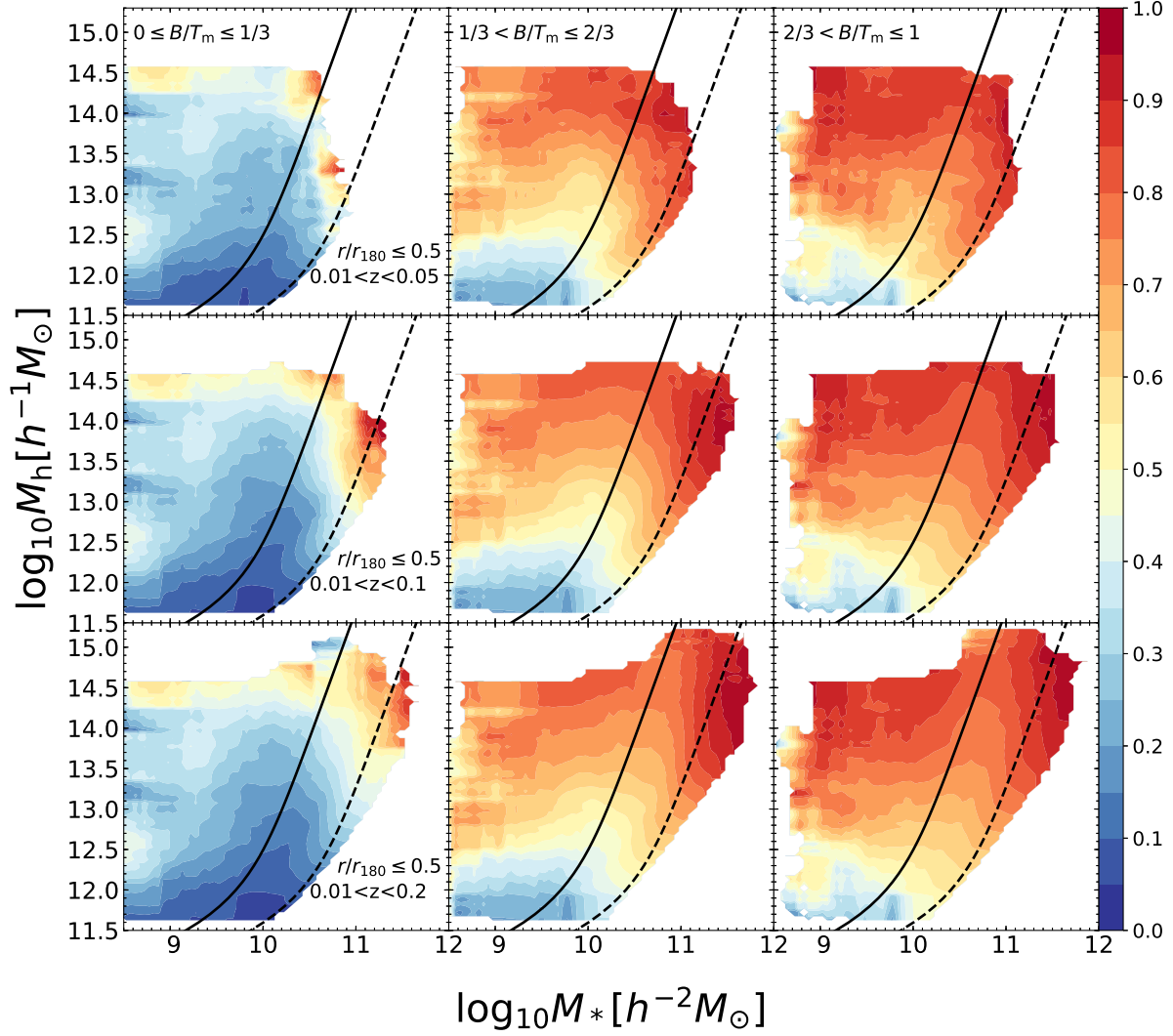


FIG. 6.— Contours show  $f_Q$  as a function of  $M_h$  and  $M_*$  for galaxies with  $r/r_{180} \leq 0.5$ . The top, middle and bottom panels show results for galaxies with  $0.01 < z < 0.05$ ,  $0.01 < z < 0.1$  and  $0.01 < z < 0.2$ , respectively. Different columns show different  $B/T_m$ , as indicated in the top panels. The results shown are smoothed on a grid with cell size given by  $\Delta \log(M_*/h^{-2}M_\odot) = 0.6$  and  $\Delta \log(M_h/h^{-1}M_\odot) = 0.6$ . Cells with less than 10 galaxies are discarded. The black solid line shows Equation (1) and the dashed line shows the central mass and halo mass relation given by Yang et al. (2009).

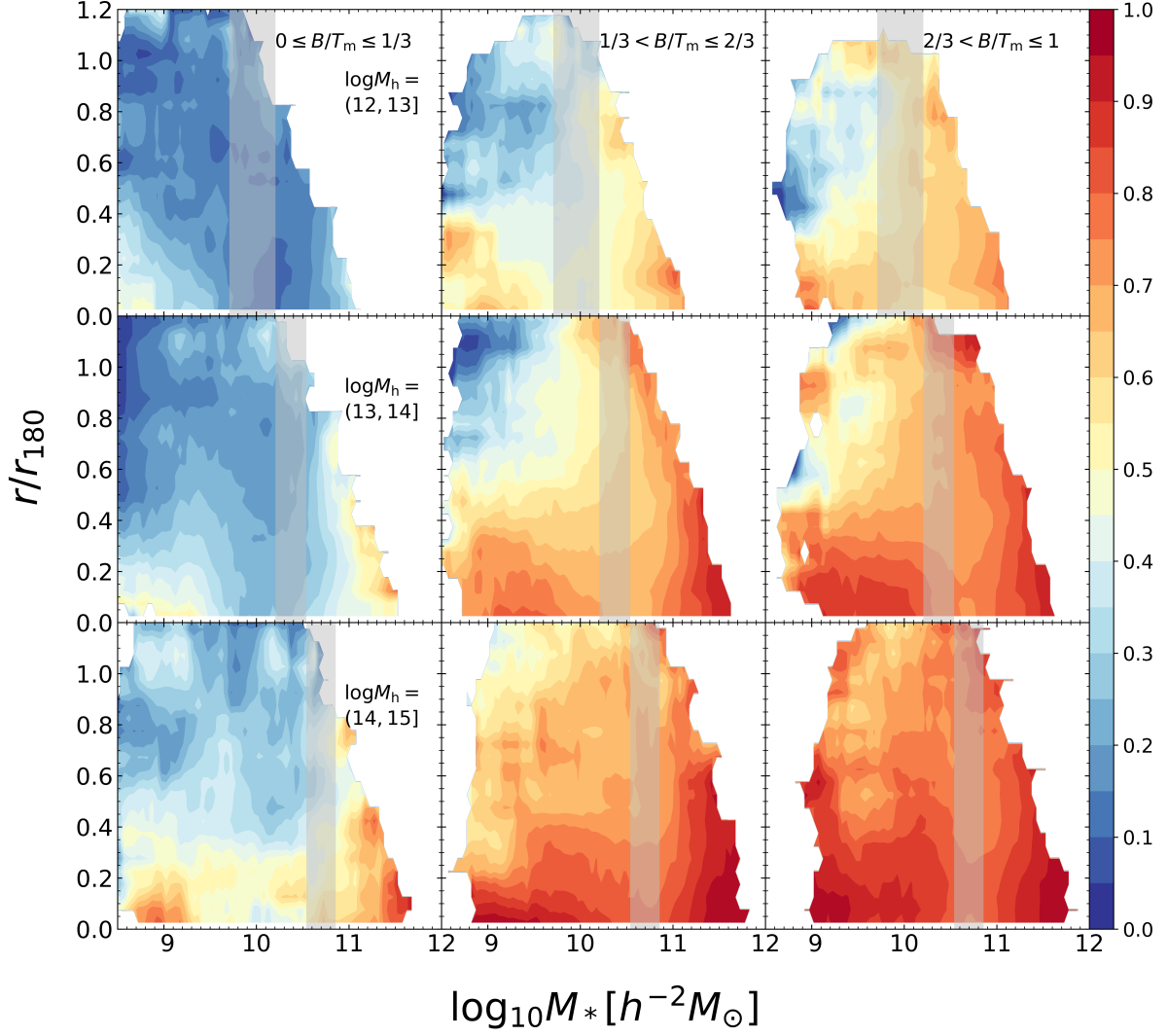


FIG. 7.— Contours show  $f_Q$  as a function of  $r/r_{180}$  and  $M_*$ . Different rows correspond to different  $M_h$  and different columns correspond to different  $B/T_m$ . The grey area in each panel shows the  $M_{*,ch}$  range corresponding to the  $M_h$  range. The grid cell size used in the plot is given by  $\Delta \log(M_*/h^{-2} M_{\odot}) = 0.6$  and  $\Delta r/r_{180} = 0.2$ ; the results are insensitive to changes in the cell size. Cells containing less than 10 galaxies are discarded.